https://doi.org/10.1016/j.ymssp.2016.05.035

Uncertainty Quantification for Acoustic Nonlinearity Parameter in Lamb Wave-Based Prediction of Barely Visible Impact Damage in Composites

Ming Hong[a,b#], Zhu Mao[b,c], Michael D. Todd[b], and Zhongqing Su[a,d*]

[a]Department of Mechanical Engineering
The Hong Kong Polytechnic University, Kowloon, Hong Kong SAR

[b]Department of Structural Engineering
University of California San Diego, La Jolla, CA, 92093, United States

[c]Department of Mechanical Engineering
University of Massachusetts Lowell, Lowell, MA, 01854, United States

[d]The Hong Kong Polytechnic University Shenzhen Research Institute
Shenzhen 518057, PR China

Submitted to *Mechanical Systems and Signal Processing*

(initially submitted on 28 August 2015; revised and re-submitted on 30 March 2016)

PhD student
* Corresponding author. Tel.: +852 2766 7818; fax: +852 2365 4703. Email: zhongqing.su@polyu.edu.hk (Prof. Zhongqing Su, *Ph.D.*)

Abstract

Nonlinear features extracted from Lamb wave signals (e.g., second harmonic generation) are demonstrably sensitive to microscopic damage such as fatigue, or material thermal degradation. While a majority of the existing studies in this context focused on detecting undersized damage in metallic materials, the present study is aimed at expanding such a detection philosophy to the domain of composites, by linking the relative acoustic nonlinearity parameter (RANP)—a prominent nonlinear signal feature of Lamb waves—to barely visible impact damage (BVID) in composites. Nevertheless, considering immense uncertainties inevitably embedded in acquired signals (due to instrumentation, environment, operation, computation/estimation, etc.) which can adversely obfuscate nonlinear features, it is necessary to quantify the uncertainty of the RANP (i.e., its statistics) in order to enhance decision-making associated with its use as a detection feature. A probabilistic model is established to numerically evaluate the statistical distribution of the RANP. Using piezoelectric wafers, Lamb waves are acquired and processed to produce histograms of RANP estimates, in both healthy and damaged conditions of a CF/EP laminate, to which the model is compared, to observe good agreement between the model-predicted and experimentally-obtained statistic distributions of the RANP. With the model, BVID in the laminate is predicted. The model is further made use of to quantify the level of confidence in damage prediction results via an algorithm based on the concept of a *receiver operating characteristic*, facilitating the practitioners to better understand the obtained results, in the presence of uncertainties.

***Keywords*:** statistical signal processing; uncertainty quantification; probabilistic modeling; relative acoustic nonlinearity parameter; Lamb waves; damage identification; composites

1. Introduction

The use of composites has become ubiquitous in modern engineering applications, ranging from large-scale fuselage panels and wings of commercial airplanes to high-performing bicycle frames and car bogies. Although endowed with numerous merits like high strength-to-weight ratio, corrosion resistance, and design flexibility, composite materials may, under inappropriate use or in harsh environment, suffer various forms of damage that are invisible and difficult to identify, primarily due to the susceptibility of composite structures to foreign object impacts [1]. For instance, a low-velocity impact, such as tool dropping during manufacturing and servicing, may result in what is commonly referred to as *barely visible impact damage* (BVID). Typical BVID ranges from indentation and matrix micro-cracks to ply delamination and fiber breakage. On top of this, cyclic loads, both mechanically and thermally, throughout the service life of a composite structure, may also lead to matrix cracking and inter-laminar damage (e.g., delamination). All these have entailed early awareness of BVID in composites and timely remediation, to prevent further material deterioration and weaken the risk of consequent system failure. Effectual damage identification can be conducive to warrant the reliability, integrity, and durability of composite structures.

Over the past few decades, a diversity of well-defined nondestructive evaluation (NDE) methods and later cutting-edge structural health monitoring (SHM) techniques have been developed, some of which are now on the verge of maturity and have been demonstrated to be capable of identifying damage in composites, including BVID, in a cost-effective manner. Of special interest are those methods taking advantage of guided ultrasonic waves (GUWs), with Lamb waves in particular [2–9]. Lamb waves feature the superior ability to interrogate a substantial area promptly with only a few transducers and low energy

consumption, the capacity to omni-directionally access hidden components (via multi-path reflections), the prospect of being implemented in an *in-situ* manner to accommodate the purposes of SHM, and most importantly, the high sensitivity to various types of damage which features a characteristic dimension comparable to the wavelength of a probing GUW (i.e., "gross" damage, such as a notch or a through-hole). A majority of the existing efforts has been focused on exploring what are referred to as *linear wave features*, which derive from linear wave propagation, dispersion, and scattering through a linear elastic medium modified by gross damage [10, 11]. As commented elsewhere [1, 11], these classical linear feature-based GUW techniques may become deficient once used to evaluate small-scale damage in inhomogeneous materials whose characteristic dimension may be much smaller than the wavelength of a probing GUW, as typified by BVID in composites; this is often the case for composite materials.

In parallel to the mainstream of using linear GUWs for developing various damage detection and health monitoring approaches, there exists a batch of studies exploring nonlinear features concealed in GUWs (e.g., sub-harmonics or second harmonics), based on the recognition that nonlinear features of GUWs, compared with their linear counterparts, can possibly be more sensitive to undersized defects or certain defect types. Representatively, Aymerich and Staszewski [12] and Meo et al. [13], respectively, evaluated BVID in composites using a cross-modulation vibro-acoustic technique (VAT) and nonlinear elastic wave spectroscopy (NEWS)—a group of methods exploiting nonlinear features of GUWs in conjunction with vibration modulation. Ciampa et al. [1] employed the mechanism of second harmonic generation in GUWs to calibrate material and damage-induced nonlinearities in a composite laminate via finite element simulation and experiment validation. Pieczonka et al. [14] also used the second harmonic generation

to examine the imaging quality of BVID and further compared the results against those from a local defect resonance (LDR) method. In another instance, Li et al. [15] explored second harmonics of Lamb waves for detecting fatigue damage in a composite panel introduced by a cyclic thermal load. In these studies, the feasibility and effectiveness of using nonlinear features of GUWs (second harmonics in particular) for damage evaluation in composites has been illustrated and validated.

Nonetheless, inherent to the use of any signal feature, whether it is linear or nonlinear, are uncertainties associated with acquired signals. The uncertainties may contaminate or even bias obtained results. Thus it becomes imperative to identify and quantify intrinsic uncertainties in measurement, experimental operation, ambient conditions, and/or computation, any of which may otherwise impair the user's ability in using the signal features properly within the context of interpretive decision-making [16]. In particular, the nonlinear contributions to the overall signal-to-noise ratio tend to be substantially lower (by orders of magnitude) than linear contributions, this further complicating an extraction and identification process. Plus, in composites, the nonlinearities can be largely multifold: even in the material's healthy state, features like voids and imperfect bonding between plies may augment the uncertainty of the said nonlinear effects. Thus, to avoid excessive Type I (false alarms) or Type II (missed calls) errors in a detection process, an uncertainty quantification model, rooted in statistical hypothesis testing, is desired. Based on this quantification, appropriate statistical inference can be reached to evaluate the health condition of a structure under inspection.

Given this backdrop, the present study establishes a probabilistic model to quantify the uncertainties of estimates of nonlinearity extracted from Lamb wave signals and to verify

the model in the context of predicting BVID in a composite laminate. A brief review of the second harmonics—one of the most representative nonlinear features of Lamb waves to be adopted in the present study—is provided in Section 2, based on which a relative acoustic nonlinearity parameter (RANP) is formulated. Section 3 derives and explores a probabilistic model for RANP estimates. Subsequently, in Section 4, experimental investigation is performed on a carbon fiber/epoxy (CF/EP) laminate plate. Miniaturized piezoelectric lead zirconate titanate (PZT) wafers are employed for actuation and acquisition of Lamb waves, which well suit the purpose of *in-situ* SHM. Continuous sine waves are generated by the PZT wafers as the input probing GUWs, and steady-state signals are acquired and processed for estimating RANP values before and after the introduction of BVID to the laminate by a drop-weight impact test. With the developed probabilistic model, histograms and predicted distributions of RANP before and after the impact test are compared. Take a step further, a receiver operating characteristic (ROC) curve is computed using the modeled RANP distributions, detailed in Section 5, which provides a quantified level of confidence in using RANP for predicting damage in the presence of uncertainty.

2. Second Harmonics of Lamb Waves

2.1 Relative acoustic nonlinearity parameter

Lamb waves refer to elastic wave propagation guided by a thin plate- or shell-like waveguide with its planar dimensions being far greater than its thickness and the wavelength of its guided wave. This kind of waveguides provides upper and lower boundaries to guide continuous propagation of Lamb waves [2]. Propagating in either symmetric or anti-symmetric modes, Lamb waves are multimodal and dispersive in nature,

usually with several modes propagating at the same time with respective velocities. Prevailing signal features of interest for the purpose of damage identification can be the delay in time-of-flight (ToF) [17–19], wave reflection/transmission [20, 21], mode conversion [3], or energy dissipation [4]. These signal features, as briefly mentioned earlier, are usually based on an assumption of linear wave propagation and linear material property changes (due to structural damage), and are therefore referred to as *linear features* in this study. The majority of existing detection techniques are based on calibrating changes in the linear features at or near the excitation frequency of the probing GUW, upon its interaction with damage.

On the contrary, *nonlinear features* of Lamb waves for damage detection generally pertain to the scenarios in which partial signal energy emerges in the frequency bands other than at the fundamental (excitation) frequency, as a consequence of energy shift under the modulation of the nonlinear effects of damage. Specifically, second harmonic generation refers to the wave energy formation at twice the excitation frequency, due to nonlinear variations of material properties (typically quadratic in nature). Theoretically, generation of second harmonics can be deemed a first-order perturbation to the linear elastic responses [22]. As a result, the solution to the nonlinear wave governing equation features two parts: the fundamental mode at the excitation frequency (denoted by f_E), plus the perturbed second harmonic mode at twice the excitation frequency ($2f_E$). The amplitudes of these two modes are related by the so-called *acoustic nonlinearity parameter*, β, which is defined as

$$\beta = \frac{A_2}{A_1^2}\frac{8}{\Omega^2 x}\gamma, \tag{1}$$

where A_1 and A_2 are the wave amplitudes at f_E and 2 f_E, respectively. Ω is the wavenumber, x the propagation distance, and γ a function depending on wave parameters

and medium properties [23], which does not vary with respect to the condition of the medium (healthy or damaged). Based on Eq. (1), the degree of the second harmonic generation (reflecting the degree of quadratic nonlinearity in the signal due to material nonlinearity and possible damage) may be determined. Normalizing β at a fixed Ω and x (while γ remains unchanged), Eq. (1) can be simplified into

$$RANP = \frac{A_2}{A_1^2}, \tag{2}$$

which, called *relative acoustic nonlinearity parameter* (RANP), represents a generalized parameter associated with nonlinear properties of Lamb waves. RANP is to be employed in this study for identification of BVID in composites.

It has been revealed in a number of studies [23–28] that the presence of small-scale damage in materials, such as fatigue cracks, thermal degradation and corrosion, generally increases local nonlinearities inherent in the damaged area of the materials. When Lamb waves traverse this area, the nonlinear distortion reflected in the acquired signals becomes more pronounced as compared to that in the pristine (healthy) condition, and this results in an increased value of the RANP. Hence, by detecting any singular increase in the RANP of Lamb wave signals, it is possible to identify small-scale damage in the waveguide.

2.2 Cumulative second harmonic generation

As pointed out earlier, the nonlinearity in a particular wave mode usually features a relatively poor signal-to-noise ratio, and therefore the acquisition of the weak second harmonic generation can be a daunting task under the interference of the multimodal and dispersive natures of Lamb waves. However, there exist certain conditions under which the probing GUW (i.e., the fundamental wave mode) is accompanied by cumulative second

harmonic generation as waves propagating: the so-called “synchronism conditions” or “internal resonance conditions” [24, 29]. A rich body of research [24, 29–31] has gone into this issue and provided the criteria of mode selection to satisfy these conditions. At a rudimentary level, by using the mode expansion method, the second harmonic wave field can be regarded as the superposition of a series of double-frequency wave modes [24]. Generally, the contribution from each double-frequency mode to the second harmonic wave field depends on its phase velocity in relation to that of the fundamental mode. If the fundamental mode and a particular double-frequency mode share the same phase velocity, internal resonance occurs, and the wave energy can be transferred from the fundamental mode to that double-frequency mode continuously as waves propagate. Other double-frequency modes would decay rapidly due to wave attenuation. Thus, by properly selecting a specific excitation frequency that enables internal resonance, cumulative second harmonics can be generated, which facilitates enhancement of the signal-to-noise ratio for damage detection purposes. Note that usually the occurrence of internal resonance also guarantees group velocity matching [30], although some debate still exists on that observation.

As far as CF/EP laminates are concerned in this study, the dispersion curves for an 8-ply CF/EP laminate with a unidirectional layup (denoted as $[0]_8$) and a thickness of 1.588 mm are shown in Fig. 1. According to the internal resonance conditions described above, the (S_1, S_2) mode pair is identified as an eligible candidate to serve cumulative second harmonic generation. As highlighted in the figure, the S_1 mode, excited at 1.460 MHz, features a phase velocity of 9,294 m/s and a group velocity of 9,265 m/s, both of which match the corresponding values of the S_2 mode at the double frequency 2.920 MHz.

3. A Probabilistic Model for RANP Estimate

According to Eq. (2), the nonlinearity of a GUW signal upon interaction with damage can be calibrated by estimating the value of ascertained RANP, once the amplitudes of the fundamental and the corresponding second harmonic modes are acquired. In practice, these two amplitudes are usually found from the signal spectrum after fast Fourier transform (FFT). Therefore, posterior to the manipulation of FFT, Eq. (2) can be rewritten as

$$RANP = \frac{A_2}{A_1^2} = \frac{\sqrt{Y_{2r}^2 + Y_{2i}^2}}{Y_{1r}^2 + Y_{1i}^2}, \tag{3}$$

where Y_{1r}, Y_{1i}, Y_{2r}, and Y_{2i} are the real and imaginary parts of the fundamental and corresponding second harmonic modes (posterior to FFT) at f_E and $2f_E$, respectively.

In this model, for a given component in the spectrum, the uncertainties in the real and imaginary parts are assumed to be random variables that follow statistically independent normal distributions. Meanwhile, these two normal distributions have the same standard deviation (σ) but different means (μ_r and μ_i): i.e., $Y_r \sim \boldsymbol{N}(\mu_r, \sigma^2)$, $Y_i \sim \boldsymbol{N}(\mu_i, \sigma^2)$, and $Y_r \perp Y_i$, as the Fourier transform maps the same original time-series signal into two orthogonal domains without discriminating the transformation gain. Here, the assumption that Y_r and Y_i share the same standard deviation will be corroborated in the subsequent experiment. With this, for the numerator, A_2, in Eq. (3), one has $Y_{2r} \sim \boldsymbol{N}(\mu_{2r}, \sigma_2^2)$ and $Y_{2i} \sim \boldsymbol{N}(\mu_{2i}, \sigma_2^2)$, where σ_2 is the common standard deviation of the second harmonic mode at $2f_E$. Hence, we define a random variable X_2 to be the square root of the sum of two normal distributions squared ($X_2 = \sqrt{Y_{2r}^2 + Y_{2i}^2}$). Mathematically, this form of random variable follows a Rice distribution, whose probability density function (PDF), denoted by $f_{X_2}(.)$, is given by

$$f_{X_2}(x_2) = \frac{x_2}{\sigma_2^2} \exp\left(-\frac{x_2^2 + \nu_n^{\,2}}{2\sigma_2^2} \right) I_0\left(\frac{x_2 \nu_n}{\sigma_2^2} \right), \tag{4a}$$

where $I_0(.)$ is the zero-order modified Bessel function of the first kind; x_2 ($x_2 \in [0, +\infty)$) is one realization of X_2 in practice; and the parameter ν_n is found by

$$\nu_n = \frac{\mu_{2r}}{\cos\left[\arctan\left(\mu_{2i} / \mu_{2r} \right) \right]} = \frac{\mu_{2i}}{\sin\left[\arctan\left(\mu_{2i} / \mu_{2r} \right) \right]}. \tag{4b}$$

Similarly, for the denominator, A_1^2, in Eq. (3), it can be hypothesized $Y_{1r} \sim \boldsymbol{N}(\mu_{1r}, \sigma_1^2)$ and $Y_{1r} \sim \boldsymbol{N}(\mu_{1r}, \sigma_1^2)$, where σ_1 is the common standard deviation of the fundamental wave mode at f_E. In order to obtain its statistical distribution, the denominator is processed as

$$A_1^2 = \sigma_1^2 \frac{A_1^2}{\sigma_1^2} = \sigma_1^2 \left[\left(\frac{Y_{1r}}{\sigma_1} \right)^2 + \left(\frac{Y_{1i}}{\sigma_1} \right)^2 \right] = \sigma_1^2 X_1, \tag{5}$$

where the sum in the square bracket, denoted as X_1 (viz., $X_1 = \frac{A_1^2}{\sigma_1^2}$), is a random variable known to follow a non-central chi-square distribution, whose PDF is given by

$$f_{X_1}(x_1) = \frac{1}{2} \exp\left(-\frac{x_1 + \lambda_n}{2} \right) \left(\frac{x_1}{\lambda_n} \right)^{k/4 - 1/2} I_{k/2-1}\left(\sqrt{\lambda_n x_1} \right), \tag{6a}$$

where x_1 ($x_1 \in [0, +\infty)$) is one realization of X_1 in practice. Since the degrees of freedom $k = 2$ in this case (one real part and one imaginary part), Eq. (6a) retreats to

$$f_{X_1}(x_1) = \frac{1}{2} \exp\left(-\frac{x_1 + \lambda_n}{2} \right) I_0\left(\sqrt{\lambda_n x_1} \right), \tag{6b}$$

where λ_n is the non-centrality parameter normalized by the standard deviation, as

$$\lambda_n = \left(\frac{\mu_{1r}}{\sigma_1} \right)^2 + \left(\frac{\mu_{1i}}{\sigma_1} \right)^2. \tag{6c}$$

At this point, the corresponding PDFs for both random variables have been obtained. Note that due to the uncertainty and measurement noise, it is highly likely that the magnitudes of the frequency components in a spectrum, respectively corresponding to fundamental and second harmonic wave modes, do not reach their maximum values at f_E and $2f_E$, respectively. Bearing this in mind, A_1 has been defined as the magnitude retrieved at exactly f_E in the spectrum in the model, instead of the largest magnitude found across the entire spectrum; likewise, A_2 is the magnitude retrieved exactly at $2f_E$, instead of the largest magnitude in the neighborhood of $2f_E$.

Now, assuming the two random variables, X_1 and X_2, do not depend on each other from the perspective of signal processing, the joint PDF of $X_1 = A_1^2 / \sigma_1^2$ and $X_2 = A_2$ may be written as

$$f_{X_1,X_2}(x_1,x_2) = \frac{x_2}{2\sigma_2^2}\exp\left(-\frac{x_1+\lambda_n}{2}-\frac{x_2^2+\nu_n{}^2}{2\sigma_2^2}\right)I_0\left(\sqrt{\lambda_n x_1}\right)I_0\left(\frac{x_2\nu_n}{\sigma_2^2}\right). \tag{7}$$

Therefore, the distribution of the ratio $R = \dfrac{X_2}{X_1} = \dfrac{A_2}{(A_1^2/\sigma_1^2)}$ is characterized as

$$\begin{aligned} f_R(r) &= \frac{d}{dr}\left[\text{Prob}\left(\frac{X_2}{X_1} < r\right)\right] = \frac{d}{dr}\left(\iint_{\frac{X_2}{X_1}<r} p_{X_1,X_2}(x_1,x_2)dx_2dx_1\right) \\ &= \frac{d}{dr}\int_0^{+\infty}\int_0^{rx_1} p_{X_1,X_2}(x_1,x_2)dx_2dx_1, \end{aligned} \tag{8}$$

where r ($r \in [0,+\infty)$) is one realization of R in practice. Finally, substituting Eq. (7) into Eq. (8) yields

$$f_R(r) = \int_0^{+\infty}\frac{x_1^2 r}{2\sigma_2^2}\exp\left(-\frac{x_1+\lambda_n}{2}-\frac{x_1^2r^2+\nu_n{}^2}{2\sigma_2^2}\right)I_0\left(\sqrt{x_1\lambda_n}\right)I_0\left(\frac{x_1\nu_n r}{\sigma_2^2}\right)dx_1. \tag{9}$$

Equation (9) does not have a known closed-form analytical solution. Instead, once the values of parameters λ_n, σ_2, and ν_n are retrieved (for example, from experimental data), this integral can be numerically evaluated.

Note that the R distribution ($R = \frac{X_2}{X_1} = \frac{A_2}{(A_1^2/\sigma_1^2)}$) is not exactly the distribution of RANP ($RANP = \frac{A_2}{A_1^2}$), as in essence a constant, σ_1^2, has been introduced to the denominator. In the following experiment, the constant σ_1^2 is chosen as the average of the variances of the real and imaginary parts. Therefore, in order to get the PDF of $RANP = \frac{A_2}{A_1^2}$ from the PDF of $R = \sigma_1^2 \frac{A_2}{A_1^2}$, a simple re-scaling process is applied, in which the R distribution is compressed by dividing R by σ_1^2, and at the same time its PDF value is multiplied by σ_1^2.

By way of illustration, Fig. 2 shows the plots of PDF and the cumulative distribution function (CDF) of the ratio R, using arbitrarily selected parametric values (λ_n = 0.6, σ_2 = 1, and ν_n = 0.5). The distribution of RANP can then be obtained by scaling the horizontal and vertical axes for this PDF by an adjusted (average) variance σ_1^2 (to be shown in subsequent figures).

4. Experimental Investigation: Model Calibration and Prediction of BVID in Composite Laminates

Note that the probabilistic model for RANP estimates, derived in Eq. (9) and shown in Fig. 2, is a generic one that is not limited to a specific material, and it is thus applicable to

composites. In this study, the model is validated using a unidirectional CF/EP laminate (made by ACP Composites, Livermore, CA, United States). In summary, under the pristine ("healthy") condition of the laminate, Lamb wave signals are acquired repeatedly (in order to ascertain the required statistical distributions), and a RANP estimate is calculated from each signal according to Eq. (2). A histogram of RANP estimates is to be plotted and compared to the predicted distribution derived from Eq. (9) (after appropriate scaling of the axes by σ_1^2 as detailed in Section 3). Then, BVID is introduced to the laminate, and the measurement process is repeated. Detailed experimental procedures are provided in the following subsections.

4.1 Healthy condition

As schematically shown in Fig. 3, the composite laminate measures 304.8×152.4×1.588 mm^3 with a layup of $[0]_8$ (tensile modulus along fiber direction: 120.66 GPa; density: 1,410 kg/m^3). Two circular PZT wafers, 10 mm in diameter each and 150 mm apart from one another, are surface-mounted on the laminate to configure a sensing path along the fiber direction, to generate and acquire GUW signals. With the reversible piezoelectric effect, each wafer can serve as an actuator or a sensor (while the other plays the opposite role). The material's dispersion curves are given in Fig. 1, and the (S_1, S_2) mode pair is selected to achieve cumulative second harmonic generation in this composite laminate, in line with the internal resonance conditions described in Section 2.2. According to the dispersion curves in Fig. 1 and the thickness of the considered laminate, the center frequency of excitation is determined to be 1.460 MHz, in order to actuate the S_1 mode in the laminate, although S_1 is only one of the multiple modes excited simultaneously at this frequency.

In order to have a stationary output signal to be acquired, a continuous sinusoidal input signal, rather than the windowed tone bursts that are commonly adopted in other linear or nonlinear GUW methods, is applied on the actuator with a function generator (Tektronix® CFG280). The preference in using a stationary output signal towards this case study resides on the consideration that it has been assumed in Section 3 that both the real and imaginary parts of an acquired signal at any frequency follow their respective normal distributions with a common standard deviation, which could be best approximated when the acquired signals are stationary, i.e., noise being time-independent. It is anticipated that this stationary input signal would lead to a steady-state sinusoidal response at the sensor, as a result of superposition of all available Lamb wave modes in the structure, including the second harmonic S_2 mode. The stationarity of the output signals from the sensor would directly determine the quality of the prediction results from the probabilistic model.

The experiment setup is photographed in Fig. 4, in which the input signal is amplified with a power amplifier (Krohn-Hite® Model 7602M) before being applied on either PZT wafer when it serves as the actuator. Output signals are acquired at the other PZT wafer with a digitizer on a PXI platform (PXI-6133) at a sampling rate of 25 MHz. In practice, wave excitation and acquisition are performed separately by the function generator and the PXI, respectively; and the input signal is channeled to another oscilloscope for reading. Through this arrangement, persistent crosstalk in the output signal can be eliminated during signal acquisition. Once the setup is complete, 500 acquisitions—each with a length of 16,384 points—are performed at random intervals, where the primary sources of uncertainties in the acquired signals are deemed from measurement and computation (such as variations in input signal generation). Then, FFT analysis is carried out to obtain 500 estimates of

RANP for the healthy condition. The detailed spectral statistics of interest are tabulated in Table 1.

It can be seen from Table 1 that at both frequencies (f_E and 2 f_E), the standard deviations of the real and imaginary parts are close to one another within four significant figures, which has validated the assumption made earlier when developing the probabilistic model in Section 3 that the real and imaginary parts of acquired signals at any frequency follow their respective normal distributions with a common standard deviation. Consequently, this enables a more accurate scaling of X_1 (the normalized squared amplitude at f_E) to A_1^2 using Eq. (5), with an average standard deviation listed in Table 1.

Figure 5 shows the normalized histogram of RANP estimates from the 500 signals acquired under the healthy condition of the laminate, superimposed with the model-predicted distribution defined by Eq. (9) using the experimentally-determined parameters as listed in Table 1 (after scaling). In the histogram, each bin is sized at 0.005. As can be seen here, the histogram matches reasonably well with the predicted uncertainty. It is noteworthy that the predicted PDF has an infinitely long tail extending to positive infinity; in contrast, the maximum RANP estimate obtained from the experiment is 0.059.

In quest of the degree of matching between the results from the experiment and from the developed model, an outlier analysis is further performed. First, the locations of percentiles of the predicted distribution are determined using Eq. (9). For example, the 95th percentile in the prediction is located at RANP = 0.0737, corresponding to a 5% level of significance as well as a 5% of outliers with respect to the overall distribution. Once the locations (i.e., RANP values) of all the percentiles of the predicted distribution are determined, the actual

outlier percentages at these RANP values are calculated for the histogram (experimental results). Figure 6 shows the plots of percentage of outliers versus level of significance from the prediction and experimental results. As can be seen in the figure, the outlier percentage of RANP estimates from the experiment (blue cross marks) is generally proportional to the significance level determined by the prediction (red dashed line). However, deviations can also be noticed, especially at lower significance levels. For instance, at the 5% level (RANP = 0.0737), no experimental RANP values are considered outliers because the maximum value observed is merely 0.059 as mentioned earlier. At the 15% level, the outlier percentage in the experiment barely exceeds 5%, falling nearly 10% short of the theoretical prediction. Such a finding can be attributable to the long tail effect of the predicted distribution. Nevertheless, for damage detection purposes in this particular application, one is mostly interested in the central tendencies of the distribution than extreme values or tail behaviors. The model, in this sense, represents the main body of the histogram rather well, which also can be visually confirmed in Fig. 5.

4.2 Damaged condition

A drop-weight impact test is performed to the above healthy laminate with a 0.3-kg impactor, which introduces BVID to the laminate. The drop height of the impactor is prudentially determined (leading to an impact energy of approximately 1.46 J). This level of energy induces BVID including matrix cracking and minor delamination in the current laminate [12], which are indeed not seen on the exterior of the laminate; whereas this amount of energy would not significantly affect the bonding conditions between the PZT wafers and the laminate which may otherwise alter the signal statistics to a great extent and reduce the repeatability of experiment. After the drop testing, the laminate is re-instrumented as described in Section 4.1, leaving all measurement settings untouched.

To verify the occurrence of the damage, a standard C-scan is performed over a 100-mm by 100-mm area in the middle of the laminate, and the scan result is shown in Fig. 7. As can be seen, slightly to the lower right of the center point, a round area of about 10.2 mm in diameter can be spotted with those pixels highlighted in gold, compared to the rest filled with green-yellow. The redder a pixel, the shorter it takes for the probing bulk wave (emitted by the C-scan device) to complete a round trip through the thickness direction at that pixel, which verifies the existence of discontinuities, or damage, in the laminate.

Once the BVID is confirmed, another set of 500 signals is acquired from the damaged laminate, and processed with exactly the same algorithm as described earlier. Figure 8 shows both the histograms and model-predicted distributions before and after the introduction of BVID into the laminate. To facilitate explicit comparison, the two histograms are plotted with the same bin size on the horizontal axis. It can be seen from the figure that the histogram in the damaged case has a “fatter”" tail, extending much further to the right than the healthy one. This represents a greater probability for the current condition of the laminate to have a larger RANP estimate relative to its healthy condition, which is consistent with the theory that the increased nonlinearities (due to the BVID) will give rise to an increased RANP estimate in general. Similarly, the two predicted distributions (blue dash-dotted line for the healthy case and red dashed line for the damaged case) also capture the above distinction.

Tables 2 and 3 list the first two moments of RANP from experimental results and from the model-predicted distributions, respectively. It can be seen in Table 2 that the introduction of BVID significantly changes the mean and sample variance of RANP estimates in

experiment. More specifically, after introduction of the BVID, the mean of RANP increases by 4.3 times, and the variance augments by a factor of 67. Again, these findings confirm that damage-induced nonlinearities would result in a larger RANP reading on average. In Table 3, the statistics from the model-predicted distributions are truncated at the 95^{th} percentile so that the effect of the infinite right tail can be partially mitigated. Although the means and variances from the predictions do not numerically match with their counterparts from the experiment (presumably due to insufficient truncation), the presence of damage in the composite laminate is observed to lift the mean significantly with a much larger variance. In fact, if the predicted distribution is truncated at a lower percentile, the tail effect can further be reduced and the order statistics would further approach the experiment results.

5. Receiver Operating Characteristics: Model Application in Uncertainty Quantification of Prediction Results

Having reached this point, the uncertainty of RANP is quantified with the developed probabilistic model, which has also been fit to the data from the experiment in the healthy and damaged cases of the laminate, as an application, respectively. Taking a step further, the developed model is subsequently made use of to quantify the level of confidence in obtained prediction results. To this end, an algorithm based on the concept of a *receiver operating characteristic* (ROC) is developed using the modeled RANP distributions. In statistics, a ROC represents a curve quantifying the confidence in a decision-making process, given a false positive rate or a tolerance level.

As illustrated in Fig. 9, suppose that the left distribution is obtained for a certain signal feature related to damage (e.g., the RANP in this study) under the healthy condition of a

structure under inspection, and the distribution on the right, which partially overlaps the left one, represents the distribution under a damaged condition. The vertical line in the middle is the decision boundary: to the left of the line, a decision of negative call (i.e., no damage) is made; to the right, a decision of positive call (i.e., damage exists) is concluded. Hence, one can define the following four damage prediction scenarios:

(i) True Positive (TP – the part of the damaged-condition distribution to the right of the decision boundary, i.e., ❶ + ❸ in Fig. 9). This means that the damage is identified truthfully (a correct decision);

(ii) False Positive (FP – the part of the healthy-condition distribution to the right of the decision boundary, i.e., ❷ + ❸). This means that damage, which does not exist actually, is falsely identified (a wrong decision);

(iii) True Negative (TN – the part of the healthy-condition distribution to the left of the decision boundary, i.e., ❹ + ❺). This means that no damage exists indeed and is hence not identified (a correct decision); and

(iv) False Negative (FN – the part of the damaged-condition distribution to the left of the decision boundary, i.e., ❺). This means that that the damage, which indeed exists, is however not identified (a wrong decision).

Having classified the possible damage prediction scenarios as above, a relationship between TP and FP can be obtained by sliding the decision boundary across the entire range of the signal feature's value (the horizontal axis), and the resulting curve is referred to as a ROC.

Figure 10 exhibits the ROC plot obtained from the model-predicted RANP distributions (the healthy versus the damaged), as represented by the two PDF curves in Fig. 8. As the

decision boundary moves from positive infinity of RANP to negative infinity (or vice versa), a combination of TP and FP rates (cumulative probabilities of RANP to the right of the decision boundary) can be obtained at every RANP reading. For example, when the decision boundary is at a large RANP value to the right of both distributions, both TP rate and FP rate are very close to 0. As the boundary moves into the damaged-state distribution but not quite into the healthy one, the TP rate starts to increase much faster than the FP rate does. Continuing this movement, the ROC curve shown in Fig. 10 in essence plots the TP rate versus the FP rate at every decision boundary (boundary values not shown here).

In practice, this ROC curve can be interpreted as follows. If one selects beforehand an acceptable FP rate, a particular RANP value associated with that FP rate then becomes the decision boundary. Any forthcoming RANP measurement that is greater than or equal to the boundary value will be called a positive detection, and otherwise negative. Following this practice with repeated RANP measurements, one is then able to expect a probability of making TP decisions that is equal to the TP rate at the selected FP rate according to the ROC curve. For instance, if one's tolerance for FP is 0.4 (a 40% FP rate), using the RANP model developed here, a TP rate of roughly 70% is anticipated with the next RANP estimate. Note that the dash-dotted line across the diagonal represents a neutral reference, meaning an equal likelihood of making a TP or an FP decision at all parameter values, which is nothing different than tossing a fair coin.

Referring back to the BVID detection in this study, it can be seen from Fig. 8 that the separation or difference between the two modeled distributions or between the two histograms are not substantially large. Especially for RANP values less than 0.02, there are considerable overlaps between the two distributions/histograms. This can be attributable to

the fact that the BVID created in the laminate is minor (hence leading to minor nonlinearities). In addition, whether the laminate is healthy or damaged, the predicted distribution also may deviate from the corresponding histogram, simply because not all assumptions made in developing the model are completely valid in reality. Hence, the ROC curve plotted in Fig. 10 serves as a conservative prediction of the TP rate at a given FP rate. In other words, given the data and the RANP model developed here, one may not be able to make a perfectly accurate damage identification decision every single time, but one is enabled to attach a quantified confidence level to decision making now, based on a selected decision boundary.

In summary, this study indeed fully demonstrates the importance of uncertainty quantification of signal features for SHM purposes. By establishing a probabilistic model for the signal feature and using tools like ROC curves, SHM practitioners can better understand what a feature estimate means for providing a quantified level of confidence in the prediction results, in the presence of uncertainties.

6. Conclusions

In this study, a nonlinear signal feature extracted from Lamb wave signals, the RANP, is employed to evaluate BVID in a CF/EP laminate. While the damage hidden inside the composites is apparently identifiable by the feature, the uncertainty inherent in RANP is modeled and scrutinized. To perform the experiment, PZT wafers are affixed to an undamaged composites sample, serving as the transducers for wave excitation and acquisition. A continuous sinusoidal signal at a selective frequency is applied, enabling cumulative second harmonic generation in the sample. A steady-state response is achieved and processed in the frequency domain to extract necessary signal features. The modeled

RANP distribution is numerically evaluated using the signal statistics, and is compared to the histogram of RANP estimates from the experiment. It has been shown that the data histograms match well with the model-predicted distributions, especially with regards to central tendencies. With BVID introduced to the composites, the new RANP distribution exhibits a fatter tail to the right, showing a greater probability of having a larger RANP estimate relative to the intact condition. This finding demonstrates the effectiveness of using RANP for detecting damage-induced nonlinearities in composite materials. Though validated using a composite panel with a unidirectional layup, it is relevant to emphasize that the probabilistic model of RANP established is independent of the material or its isotropy; the model can be extended to composites with arbitrary fiber orientation as long as the dispersive properties of the Lamb waves in the concerned composites available.

Using the proposed RANP distribution model, a ROC curve is plotted to indicate the level of confidence in making TP detections at an accepted FP rate. While the ROC curve obtained from the modeled distribution indicates only moderate levels of confidence in using RANP for BVID detection in this specific example, the existence of an uncertainty model nevertheless provides a quantified reliability measure of RANP for other scenarios of damage detection and SHM, where second harmonic Lamb waves are of interest.

Acknowledgments

This project is jointly supported by the Hong Kong Research Grants Council via General Research Funds (No. 523313 and No. 15214414), National Natural Science Foundation of China (Grant No. 51375414), the research grant (UD130058JD) of the Agency for Defense Development of the Korean government, and the Leading Foreign Research Institute Recruitment Program through the National Research Foundation of Korea funded by the

Ministry of Science, ICT and Future Planning (2011-0030065). The first author would like to acknowledge the Fulbright-RGC Hong Kong Research Scholar Award. The authors are also grateful to Prof. Hyonny Kim and Dr. Zhi Chen for their assistance in implementing the C-scan said in the paper.

References

1. F. Ciampa, E. Onder, E. Barbieri, M. Meo, Detection and modelling of nonlinear elastic response in damaged composite structures, J. Nondestruct. Eval. 33 (2014) 515–521 (2014).
2. Z. Su, L. Ye, Y. Lu, Guided Lamb waves for identification of damage in composite structures: A review, J. Sound Vib. 295 (2006) 753–780.
3. C. Ramadas, K. Balasubramaniam, M. Joshi, C.V. Krishnamurthy, Interaction of guided Lamb waves with an asymmetrically located delamination in a laminated composite plate, Smart Mater. Struct. 19 (2010) 065009.
4. Z. Wu, X.P. Qing, F.K. Chang, Damage detection for composite laminate plates with a distributed hybrid PZT/FBG sensor network, J. Intell. Mater. Syst. Struct. 20 (2009) 1069–1077.
5. P.B. Dao., W.J. Staszewski, Lamb wave based structural damage detection using cointegration and fractal signal processing, Mech. Syst. Signal Proc. 49 (2014) 285–301.
6. C.M. Yeum, H. Sohn, J.B. Ihn., H.J. Lim, Instantaneous delamination detection in a composite plate using a dual piezoelectric transducer network, Compos. Struct. 94 (2012) 3490–3499.
7. Z. Su, C. Yang, N. Pan, L. Ye, L.-M. Zhou, Assessment of delamination in composite beams using shear horizontal (SH) wave mode, Compos. Sci. Technol. 67 (2007) 244–251.
8. O. Mesnil, C.A.C. Leckey, M. Ruzzeno, Instantaneous and local wavenumber estimations for damage quantification in composites, Struct. Health Monit. 14 (2015) 193–204.
9. R. Watkins, R. Jha, A modified time reversal method for Lamb wave based diagnostics of composite structures, Mech. Syst. Signal Proc. 31 (2012) 345–354.

10. Y. Lu, L. Ye, Z. Su, L. Zhou, L. Cheng, Artificial neural network (ANN)-based crack identification in aluminum plates with Lamb wave signals, J. Intell. Mater. Syst. Struct. 20 (2009) 39–49.
11. Z. Su, C. Zhou, M. Hong, L. Cheng, Q. Wang, X. Qing, Acousto-ultrasonics-based fatigue damage characterization: Linear versus nonlinear signal features, Mech. Syst. Signal Proc. 45 (2014) 225–239.
12. F. Aymerich, W.J. Staszewski, Experimental study of impact-damage detection in composite laminates using a cross-modulation vibro-acoustic technique, Struct. Health Monit. 9 (2010) 541–553.
13. M. Meo, U. Polimeno, G. Zumpano, Detecting damage in composite material using nonlinear elastic wave spectroscopy, Appl. Compos. Mater. 15 (2008) 115–126.
14. L. Pieczonka, A. Klepka, W.J. Staszewski, T. Uhl, Nonlinear acoustic imaging of structural damages in laminated composites, Proc. 7th EWSHM (2014) 1670–1675.
15. W. Li, Y. Cho, J.D. Achenbach, Detection of thermal fatigue in composites by second harmonic Lamb waves, Smart Mater. Struct. 21 (2012) 085019.
16. Z. Mao, M. Todd, A model for quantifying uncertainty in the estimation of noise-contaminated measurements of transmissibility, Mech. Syst. Signal Proc. 28 (2012) 470–481.
17. W. Ostachowicz, P. Kudela, P. Malinowski, T. Wandowski, Damage localization in plate-like structures based on PZT sensors, Mech. Syst. Signal Process. 23 (2009) 1805–1829.
18. T. Kundu, H. Nakatani, N. Takeda, Acoustic source localization in anisotropic plates, Ultrasonics 52 (2012) 740–746.
19. T. Clarke, P. Cawley, P.D. Wilcox, A.J. Croxford, Evaluation of the damage detection capability of a sparse-array guided-wave SHM system applied to a complex structure under varying thermal conditions, IEEE Trans. Ultrason. Ferroelectr. Freq. Control 56 (2009) 2666–2678.

20. J.E. Michaels, Detection, localization and characterization of damage in plates with an in situ array of spatially distributed ultrasonic sensors, Smart Mater. Struct. 17 (2008) 035035.
21. Y.L. Koh, W.K. Chiu, N. Rajic, Effects of local stiffness changes and delamination on Lamb wave transmission using surface-mounted piezoelectric transducers, Compos. Struct. 57 (2002) 437–443.
22. S.M. Liu, S. Best, S.A. Neild, A.J. Croxford, Z. Zhou, Measuring bulk material nonlinearity using harmonic generation, NDT E Int. 48 (2012), 46–53.
23. Y. Xiang, M. Deng, F.-Z. Xuan, C.-J. Liu, Experimental study of thermal degradation in ferritic Cr-Ni alloy steel plates using nonlinear Lamb waves, NDT E Int. 44 (2011) 768–774.
24. M. Deng, J. Pei, Assessment of accumulated fatigue damage in solid plates using nonlinear Lamb wave approach, Appl. Phys. Lett. 90 (2007) 121902.
25. K.-Y. Jhang, Nonlinear ultrasonic techniques for nondestructive assessment of micro damage in material: A review, Int. J. Precis. Eng. Man. 10 (2009) 123–135.
26. C. Zhou, M. Hong, Z. Su, Q. Wang, L. Cheng, Evaluation of fatigue cracks using nonlinearities of acousto-ultrasonic waves acquired by an active sensor network, Smart Mater. Struct. 22 (2013) 015018.
27. C. Pruell, J.Y. Kim, J. Qu, L.J. Jacobs, Evaluation of fatigue damage using nonlinear guided waves, Smart Mater. Struct. 18 (2009) 035003.
28. M. Hong, Z. Su, Y. Lu, H. Sohn, X. Qing, Locating fatigue damage using temporal signal features of nonlinear Lamb waves, Mech. Syst. Signal Proc. 60-61 (2015) 182–197.
29. J.L. Rose, Ultrasonic Guided Waves in Solid Media, Cambridge University Press, New York, 2014.
30. N. Matsuda, S. Biwa, Phase and group velocity matching for cumulative harmonic generation in Lamb waves, J. Appl. Phys. 109 (2011) 094903.

31. V.K. Chillara, C.J. Lissenden, Interaction of guided wave modes in isotropic nonlinear elastic plates: higher harmonic generation, J. Appl. Phys. 111(2012) 124909.

A List of Table and Figure Captions

TN = ❹ + ❺, and FN = ❺

Figure 10 Receiver operating characteristic (ROC) curve showing TP Rate versus FP Rate at every RANP value, predicted by the modeled distributions (the red dashed curve for the damaged and the blue dash-dotted curve for the healthy in Fig. 8)

Table 1 Spectral statistics of the 500 signals acquired under the healthy condition of the laminate in the experiment

FFT Frequency (f_E)	Real Mean μ_{1r}	Imag. Mean μ_{1i}	Real Std. Dev. σ_{1r}	Imag. Std. Dev. σ_{1i}	Avg. Std. Dev. σ_1	λ_n
1.461 MHz	0.0080	-9.953×10^{-4}	0.3894	0.3903	0.3898	4.297×10^{-4}
FFT Frequency ($2f_E$)	Real Mean μ_{2r}	Imag. Mean μ_{2i}	Real Std. Dev. σ_{2r}	Imag. Std. Dev. σ_{2i}	Avg. Std. Dev. σ_2	ν_n
2.922 MHz	4.598×10^{-5}	-1.052×10^{-4}	9.048×10^{-4}	9.323×10^{-4}	9.185×10^{-4}	1.148×10^{-4}

Table 2 Sample means and variances of RANP estimates from the experiment

Sample Condition	Mean	Variance
Healthy	0.00755	6.794×10^{-5}
Damaged	0.03269	4.551×10^{-3}

Table 3 Sample means and variances of RANP estimates from the distribution model

Sample Condition	Mean	Variance
Healthy	0.0158	1.503×10^{-3}
Damaged	0.0449	2.153×10^{-2}

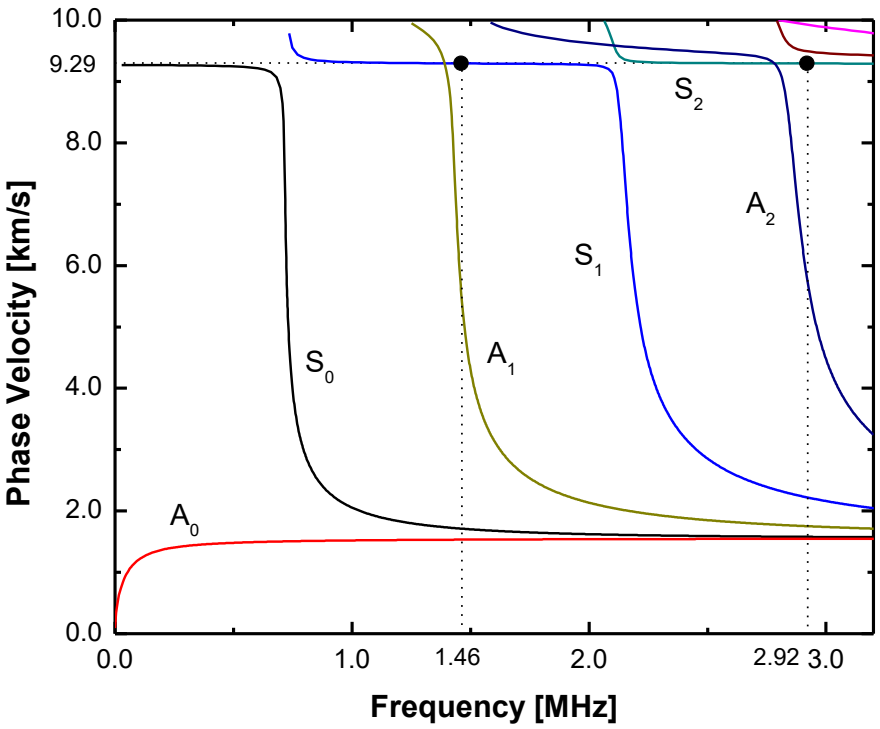

(a)

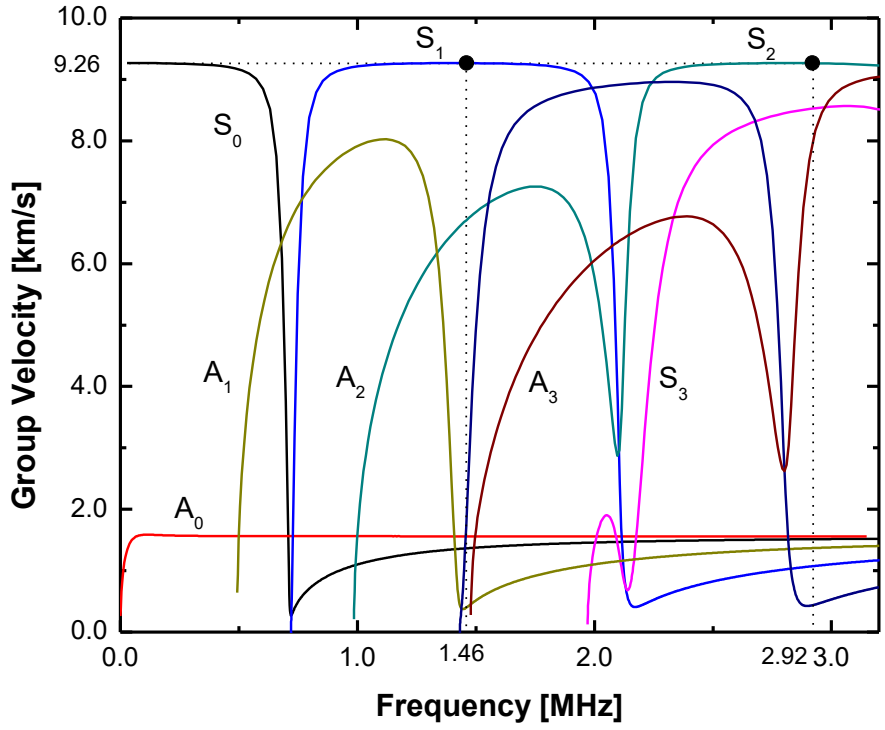

(b)

Figure 1 Dispersion curves of Lamb waves in $[0]_8$ CF/EP laminate with 1.588 mm in thickness: (a) phase velocities versus frequency; and (b) group velocities versus frequency (mode pair (S_1, S_2) marked as the candidate for cumulative second harmonic generation)

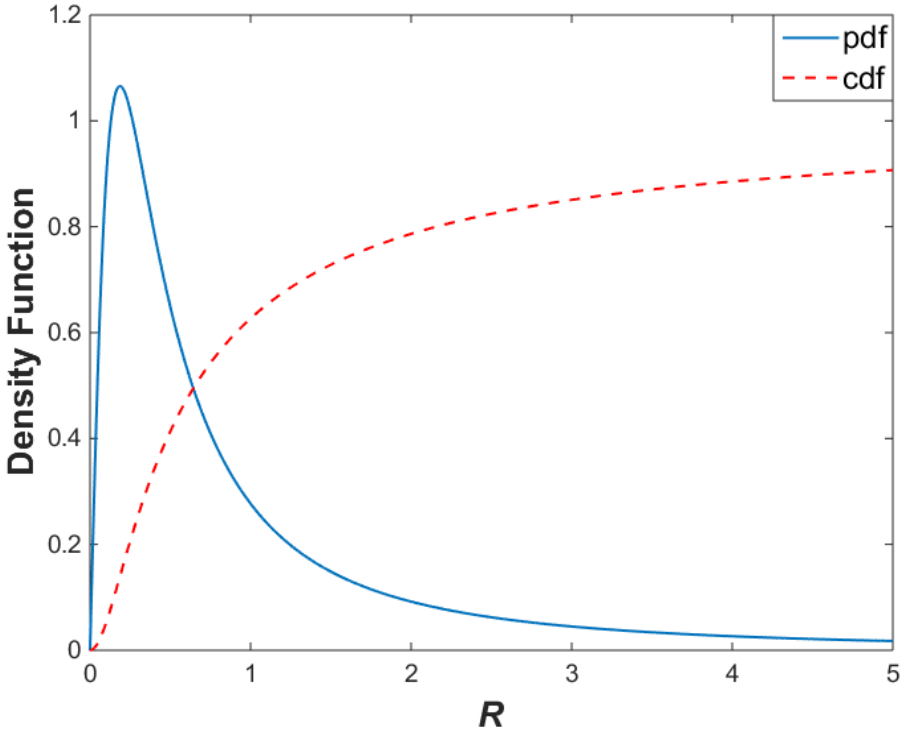

Figure 2 PDF and CDF of R, with $\lambda_n = 0.6$, $\sigma_2 = 1$, and $v_n = 0.5$

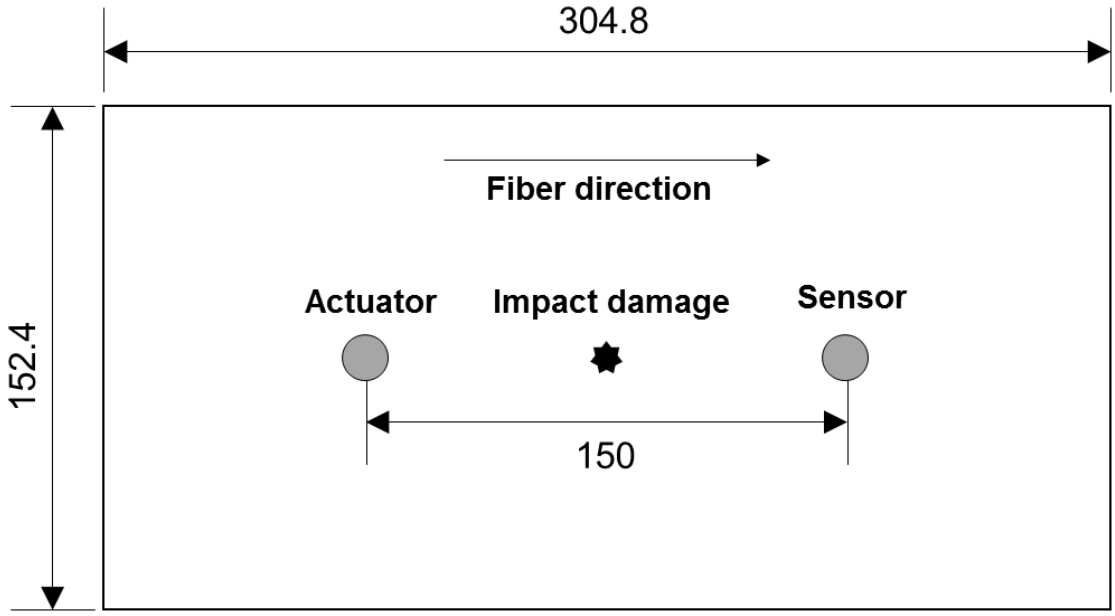

Figure 3 Schematic diagram of the CF/EP laminate in experimental investigation (impact to be introduced later targeted at the middle point of the sensing path; dimensions displayed in mm)

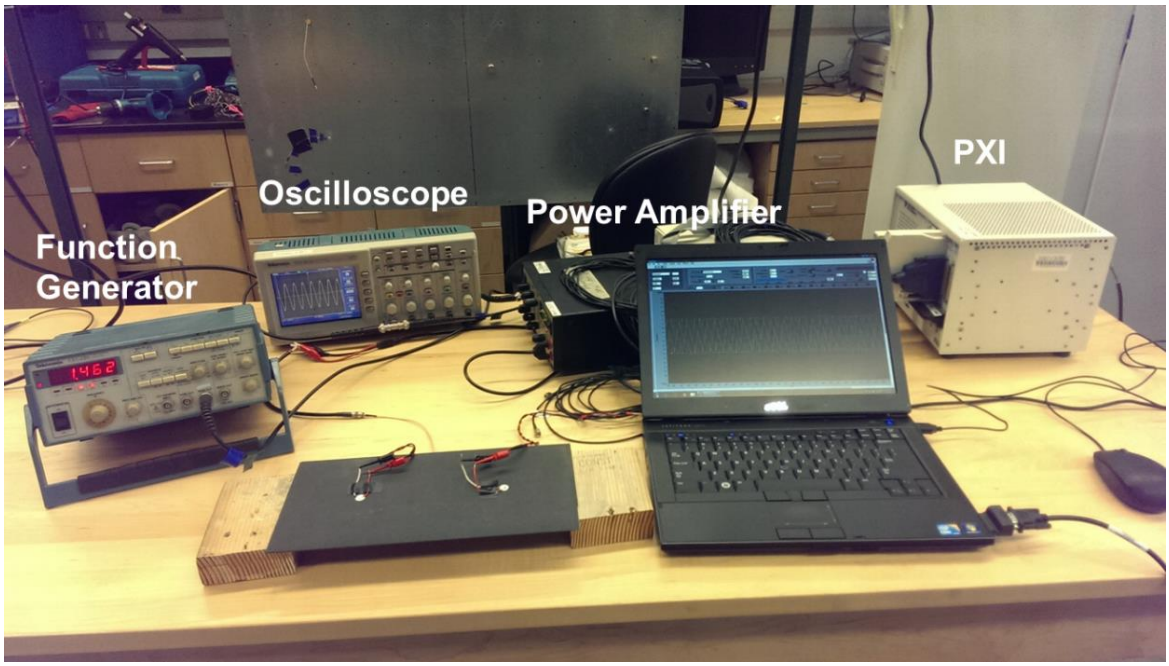

Figure 4 Experimental setup

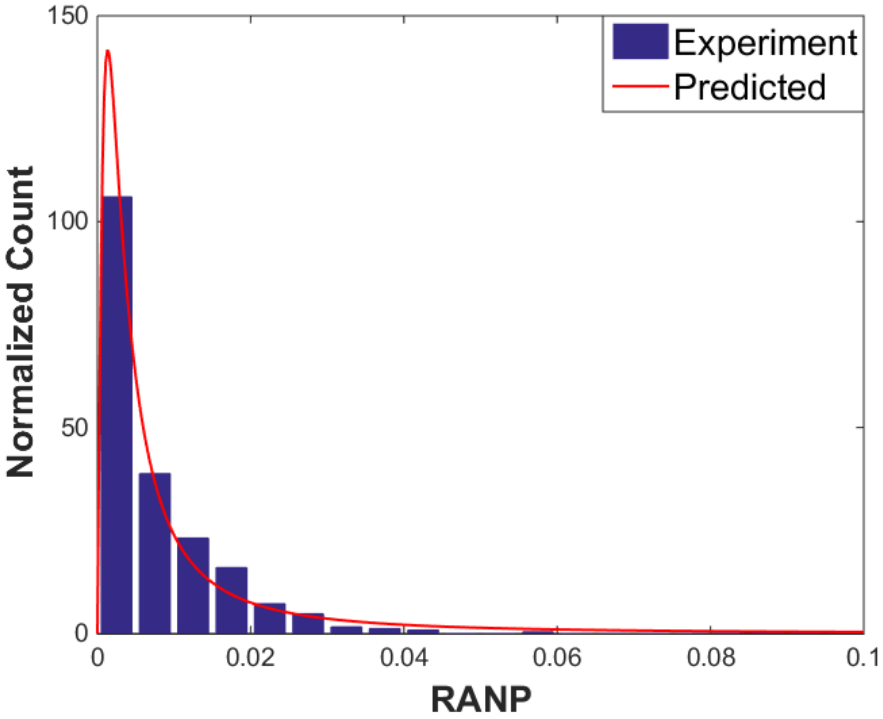

Figure 5 Histogram of RANP estimates from experiment under the healthy condition versus model-predicted distribution obtained from Eq. (9)

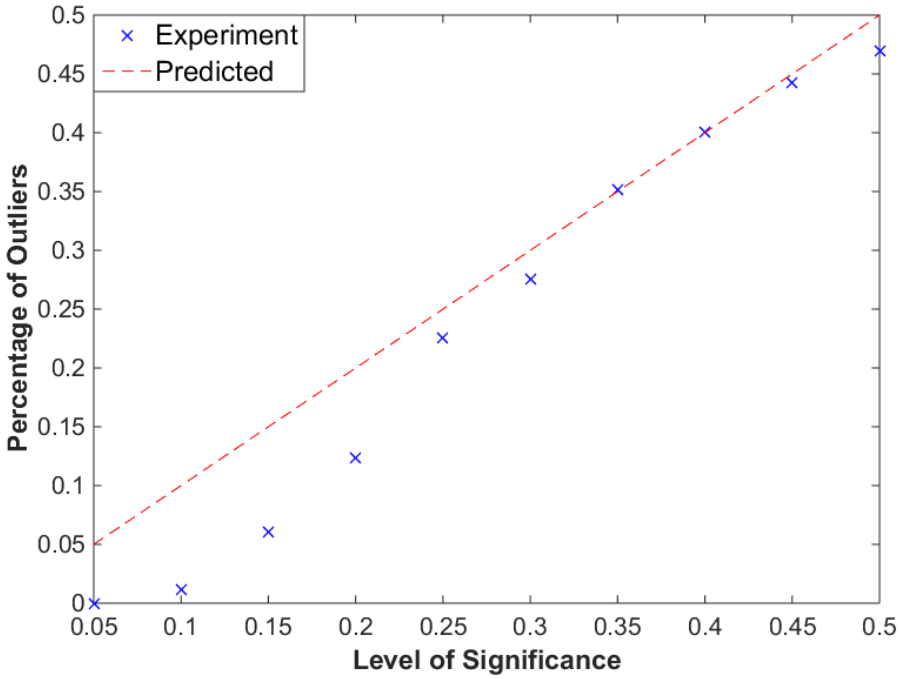

Figure 6 Percentage of outliers against level of significance, from the model-predicted distribution and experiment

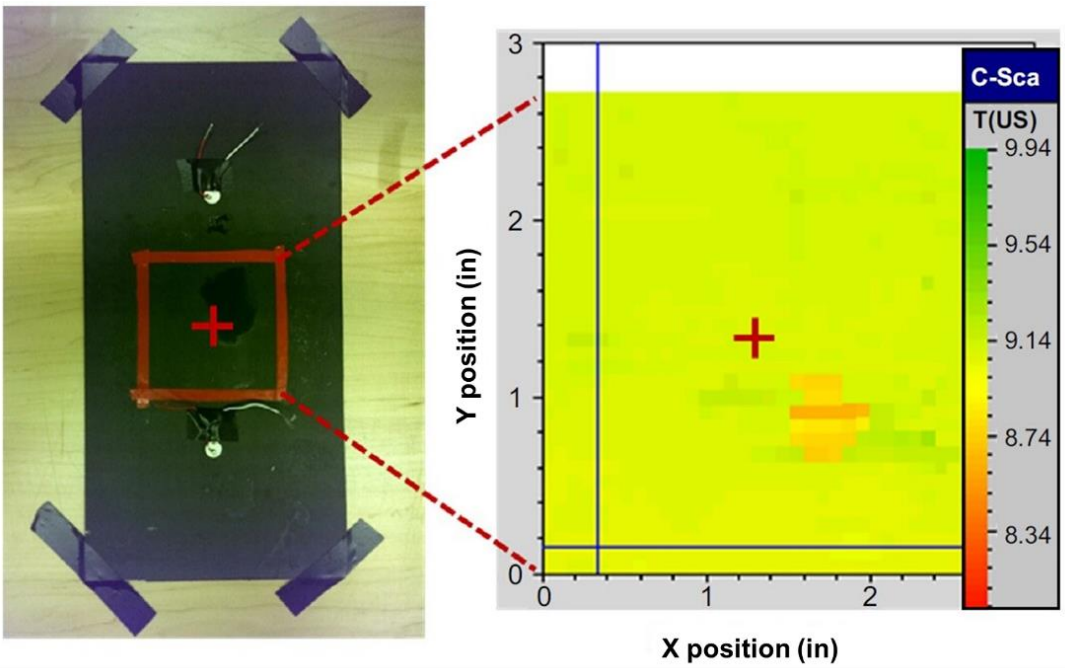

Figure 7 C-scan image of the laminate sample (showing the central part only) revealing the location of the BVID, which is highlighted in orange with smaller ToF values for the probing bulk wave to finish a round trip from the top surface to the damaged layer (as opposed to the rest where the wave travels between the top and bottom surfaces of the laminate)

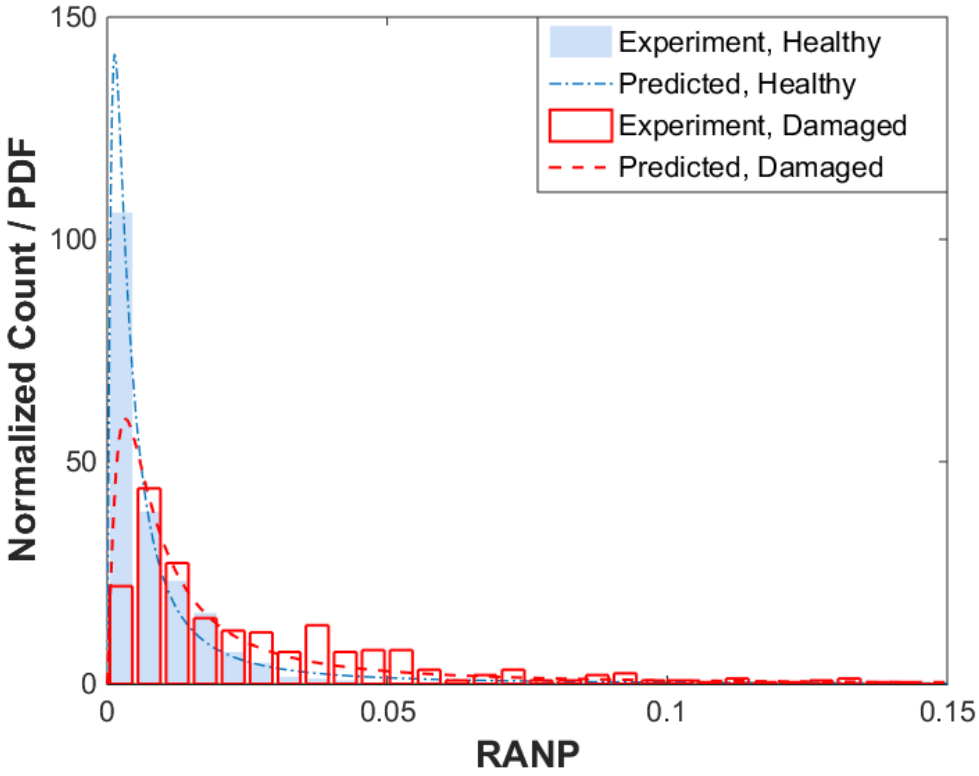

Figure 8 Histograms of RANP estimates and model-predicted distributions before and after introduction of the BVID

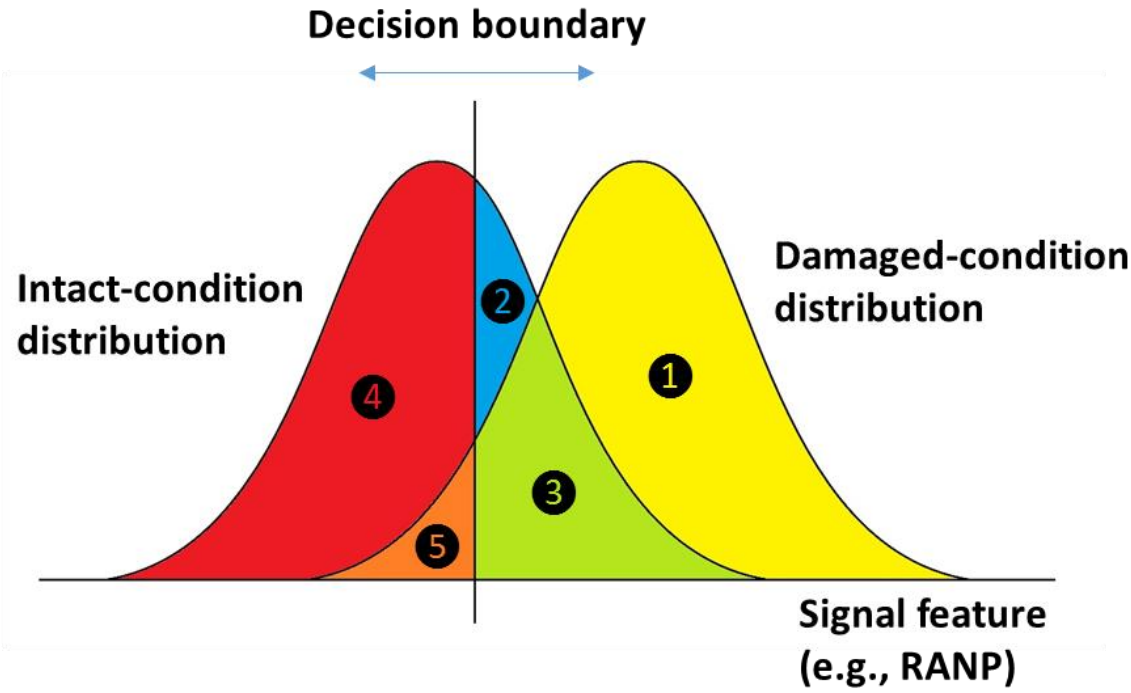

Figure 9 Illustration of TP, FP, TN, and FN with respect to a moving decision boundary between the feature distributions: TP = ❶ + ❸, FP = ❷ + ❸, TN = ❹ + ❺, and FN = ❺

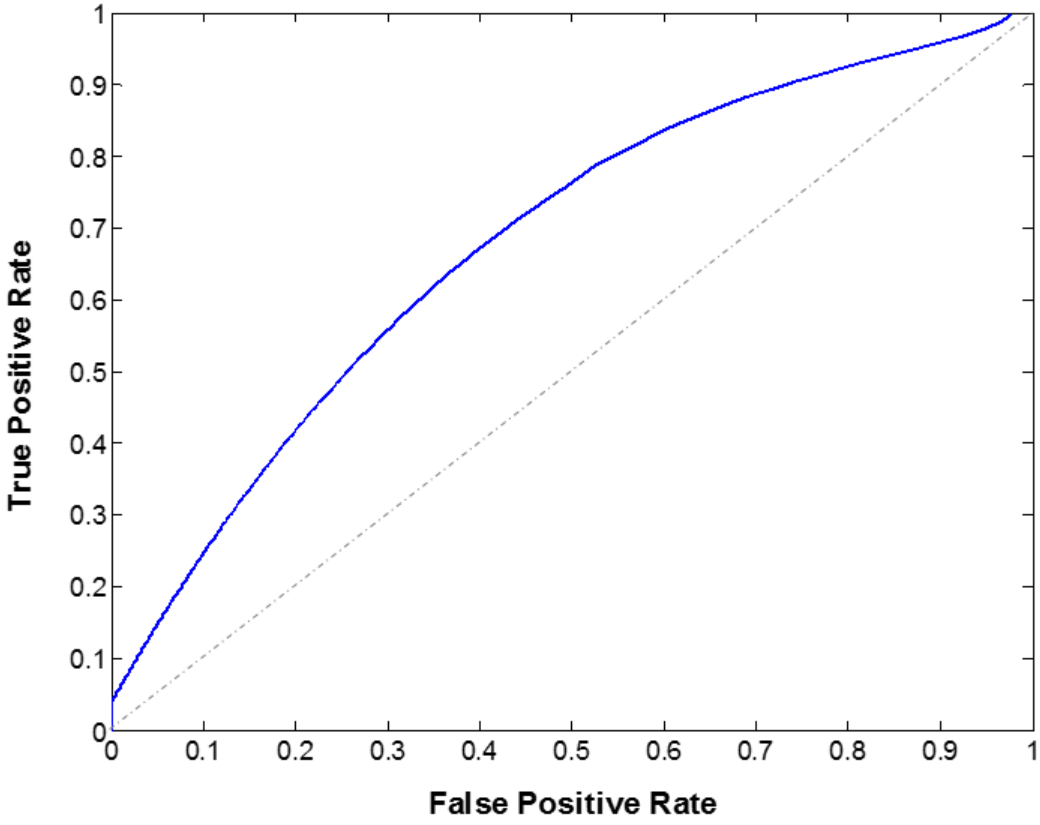

Figure 10 Receiver operating characteristic (ROC) curve showing TP Rate versus FP Rate at every RANP value, predicted by the modeled distributions (the red dashed curve for the damaged and the blue dash-dotted curve for the healthy in Fig. 8)